The Astrophysical Journal, 836:129 (15pp), 2017 February 10 doi:10.3847/1538-4357/836/1/129

A Massive Shell of Supernova-formed Dust in SNR G54.1+0.3

Tea Temim[1], Eli Dwek[2], Richard G. Arendt[2,3], Kazimierz J. Borkowski[4], Stephen P. Reynolds[4], Patrick Slane[5], Joseph D. Gelfand[6], and John C. Raymond[5]
[1] Space Telescope Science Institute, 3700 San Martin Drive, Baltimore, MD 21218, USA
[2] Observational Cosmology Lab, Code 665, NASA Goddard Space Flight Center, Greenbelt, MD 20771, USA
[3] University of Maryland-Baltimore County, Baltimore, MD 21250, USA
[4] North Carolina State University, Raleigh, NC 27695, USA
[5] Harvard-Smithsonian Center for Astrophysics, 60 Garden Street, Cambridge, MA 02138, USA
[6] New York University, Abu Dhabi, UAE
Received 2016 November 4; revised 2017 January 2; accepted 2017 January 3; published 2017 February 13

Abstract

While theoretical models of dust condensation predict that most refractory elements produced in core-collapse supernovae (SNe) efficiently condense into dust, a large quantity of dust has so far only been observed in SN 1987A. We present an analysis of observations from the *Spitzer Space Telescope*, *Herschel Space Observatory*, Stratospheric Observatory for Infrared Astronomy, and *AKARI* of the infrared shell surrounding the pulsar wind nebula in the supernova remnant G54.1+0.3. We attribute a distinctive spectral feature at 21 μm to a magnesium silicate grain species that has been invoked in modeling the ejecta-condensed dust in Cas A, which exhibits the same spectral signature. If this species is responsible for producing the observed spectral feature and accounts for a significant fraction of the observed infrared continuum, we find that it would be the dominant constituent of the dust in G54.1+0.3, with possible secondary contributions from other compositions, such as carbon, silicate, or alumina grains. The total mass of SN-formed dust required by this model is at least 0.3 $M_{\odot}$. We discuss how these results may be affected by varying dust grain properties and self-consistent grain heating models. The spatial distribution of the dust mass and temperature in G54.1+0.3 confirms the scenario in which the SN-formed dust has not yet been processed by the SN reverse shock and is being heated by stars belonging to a cluster in which the SN progenitor exploded. The dust mass and composition suggest a progenitor mass of 16–27 $M_{\odot}$ and imply a high dust condensation efficiency, similar to that found for Cas A and SN 1987A. The study provides another example of significant dust formation in a Type IIP SN explosion and sheds light on the properties of pristine SN-condensed dust.

Key words: dust, extinction – ISM: general – ISM: individual objects (SNR G54.1+0.3) – ISM: supernova remnants – pulsars: individual (PSR J1930+1852)

1. Introduction

Interstellar dust plays a significant role in virtually all processes governing the evolution of galaxies and is a key ingredient in chemical evolution models and feedback processes important for star formation. Dust can be produced in the stellar wind outflows of massive stars and in the ejecta of core-collapse supernova (SN) explosions. However, the quantity and relative fraction of dust formed in these sources are still not well understood. The question of whether SN explosions are primary sources of dust in the universe is still under debate. High dust masses observed in high-redshift galaxies suggest that large quantities of dust had to form on timescales of only a few hundred million years (e.g., Dwek & Cherchneff 2011; Gall et al. 2011; Valiante et al. 2011; Dwek et al. 2015; Michałowski 2015), pointing to core-collapse SNe as the most likely sources. Dwek et al. (2007) find that an average SN explosion would need to produce anywhere from 0.1 to 1.0 $M_{\odot}$ of dust in order to explain the observed dust mass of $>10^8\,M_{\odot}$ in the galaxy SDSS J1148+5251 at a redshift of 6.4. The range of required masses is strongly dependent on the efficiency of dust destruction in the interstellar medium (ISM) of the galaxy.

Theoretical models of dust formation using classical nucleation theory and the chemical kinematic approach for the formation of molecular precursors do indeed predict that 0.03–0.7 $M_{\odot}$ of dust can form in the ejecta of core-collapse SNe, and that the grain properties and masses depend on factors such as the type of SN explosion, the mass of the SN progenitor, metallicity, and clumping and mixing of the SN ejecta (e.g., Todini & Ferrara 2001; Cherchneff & Dwek 2009, 2010; Kozasa et al. 2009; Sarangi & Cherchneff 2013, 2015). However, observations of supernova remnants (SNRs) and extragalactic SNe in the mid-infrared (IR) have generally revealed dust masses that are orders of magnitude lower, in the range of 10^{-2}–$10^{-3}\,M_{\odot}$ (see Gall et al. 2011 for a review). While it was hypothesized that a large mass of SN dust may be cooler and emitting primarily at far-IR wavelengths, the lack of sensitivity and spatial resolution, in addition to high confusion noise, prohibited clear detections of SN-formed dust in many SNe and SNRs.

Far-IR *Herschel* observations provided evidence for a significant amount of dust in only three SNRs: the Crab Nebula, Cas A, and SN 1987A. The dust mass in the Crab Nebula is estimated to be between 0.02 and 0.3 $M_{\odot}$ (Gomez et al. 2012; Temim & Dwek 2013; Owen & Barlow 2015), while the current mass in Cas A is $\sim$0.1 $M_{\odot}$ (Barlow et al. 2010; Sibthorpe et al. 2010; Arendt et al. 2014), with 0.8–1.0 $M_{\odot}$ predicted to have formed initially, before being sputtered away by the SN reverse shock (Micelotta et al. 2016).

Herschel observations of SN 1987A led to an exciting discovery of a significant mass of dust that likely formed in the SN ejecta (Matsuura et al. 2011). The ejecta origin was later confirmed with Atacama Large Millimeter/submillimeter

Array (ALMA) observations (Indebetouw et al. 2014). The latest estimate indicates that at least $\sim 0.5\,M_{\odot}$ of dust formed in the explosion. However, the composition of the dust is still a matter of debate (Dwek & Arendt 2015; Matsuura et al. 2015; Wesson et al. 2015), and how much will eventually survive the passage of the SN reverse shock is still unknown.

In this paper, we present a follow-up study of the dusty shell in the SNR G54.1+0.3, indicating that this system contains a significant mass of SN-formed dust. G54.1+0.3 contains a pulsar wind nebula (PWN) with a well-defined jet and torus structure, exhibiting properties similar to the Crab Nebula (Lu et al. 2001; Temim et al. 2010). The age of the system is estimated to be 1500–3000 yr (Chevalier 2005; Bocchino et al. 2010; Gelfand et al. 2015). Based on the spectral types of stars in the surrounding stellar cluster, Kim et al. (2013) constrain the range of the progenitor mass to be 18–35 $M_{\odot}$, which likely resulted in a Type IIP SN explosion. This range overlaps with the results of Gelfand et al. (2015), who derived a progenitor mass of 15–20 $M_{\odot}$ using a model for the dynamical and radiative evolution of a PWN inside an SNR.

The *Spitzer* mid-IR images of this system revealed a shell of emission surrounding the PWN and a dozen point sources embedded in the shell with an apparent 24 μm IR excess. Due to this excess, the point sources were originally attributed to young stellar objects (YSOs) whose formation was triggered by the progenitor star (Koo et al. 2008). However, the analysis of line emission detected with the Infrared Spectrograph (IRS) aboard *Spitzer* revealed that the shell has a high expansion velocity of up to 500 km s^{-1} and that the emission likely originates from SN ejecta. The IR excess in the point sources can be attributed to SN-formed dust that is heated to higher temperatures as it blows past early-type stars that are members of the cluster in which the SN exploded (Temim et al. 2010). Kim et al. (2013) used near-IR spectroscopic observations of the stellar sources to determine their spectral types and concluded that they are indeed late O- or early B-type stars that show no evidence for emission lines that are often present in Herbig Ae/Be stars. Kim et al. (2013) also also constrained the distance to G54.1+0.3 by calculating the photometric distances to the stars in the shell based on temperatures fitted to their spectral energy distributions (SEDs). Their derived distance range is 4.6–8.1 kpc, with an average of 6.0 ± 0.4 kpc.

In this paper, we analyze the mid- and far-IR emission from the shell surrounding the PWN in G54.1+0.3 using observations from the *Spitzer Space Telescope*, *Herschel Space Observatory*, Stratospheric Observatory for Infrared Astronomy (SOFIA), and *AKARI* in order to confirm the origin and determine the properties of the dust in the IR shell.

2. Observations and Data Reduction

2.1. Spitzer Observations

This work includes *Spitzer* imaging and spectroscopy that were previously analyzed and presented in Temim et al. (2010). We include the Multiband Imaging Photometer (MIPS) 24 μm image taken on 2005 May 15 under the program ID 3647 (PI: Slane), and the *Spitzer* IRS (Houck et al. 2004) high-resolution spectra taken at two different positions on the IR shell, which are indicated by the white boxes in Figure 1. Position 1 is located at the interface of the IR shell and the pulsar's jet seen in X-rays, while position 2 is located at the brightest peak in the 24 μm image, which Temim et al. (2010) call the "IR knot." The reduction of the *Spitzer* observations is discussed in detail in Temim et al. (2010).

2.2. Herschel Observations

Herschel imaging of G54.1+0.3 was obtained with the Photodetector Array Camera (PACS; Poglitsch et al. 2010) at 70, 100, and 160 μm and the Spectral and Photometric Imaging Receiver (SPIRE; Griffin et al. 2010) at 250, 350, and 500 μm. The PACS observations were performed on 2011 November 5 using the "scan map" mode and a scan speed of 20 arcsec s^{-1} (proposal ID: *OT1_ttemim_1*, observation IDs: 1342231919–1342231922). The SPIRE observations were performed on 2011 May 2 and October 23 in the "parallel mode," under the proposal ID *KPOT_smolinar_1* (observation IDs: 1342219812, 1342219813, 1342231341, and 1342231342). The imaging observations were processed and reduced with the *Herschel* Interactive Processing Environment (HIPE; Ott 2010) version 14.0.0 and images produced using the *MADmap* software (Cantalupo et al. 2010). The resulting PACS and SPIRE images are in units of Jy/pixel with pixel scales (FWHM) of 1.6, 1.6, 3.2, 6, 10, and 14″/pixel (6″, 8″, 12″, 18.″1, 24.″9, and 36.″4) for the 70, 100, 160, 250, 350, and 500 μm images, respectively. The calibration uncertainties for the PACS and SPIRE images are assumed to be 10% and 7%, respectively.

Herschel spectra were obtained with the PACS Integral Field Unit (IFU) Spectrometer (Poglitsch et al. 2010) in the "range spectroscopy" mode, covering the lines of [O I] at 63.18 and 145.53 μm, [O III] at 88.36 μm, and [C II] at 157.74 μm. The IFU has 5 × 5 spaxels, measuring 9.″4 on a side, and the G54.1+0.3 shell was mapped in nine pointings (3 × 3 grid), with an additional pointing for the off-source background. The level 2 data were analyzed using HIPE version 14.0.0. The observations were used to determine whether the line emission contributes significantly to the integrated fluxes measured from the *Herschel* images.

2.3. SOFIA Imaging

G54.1+0.3 was observed by SOFIA on 2016 February 18 (OC4-A Flight 8), using the Faint Object infraRed CAmera for the SOFIA Telescope (FORCAST). Simultaneous imaging in the short- and long-wavelength channels, using a cold dichroic beamsplitter, was done in F197 (+F315) and F253 (+F348) broadband filters with effective wavelengths of 19.7 (31.5) and 25.3 (34.8) μm, and bandwidths of 5.5 (1.86) 5.7 (3.8) μm, respectively. G54.1+0.3 is an extended (2.′5 in size) IR source that fits nicely into the 3.′4 × 3.′2 FORCAST field of view. Chopping and nodding were done symmetrically about the telescope's optical axis, using symmetric nod–match–chop with a 2.′5 chop throw (the nod throw is matched to the chop throw in this chopping and nodding mode). This fairly large chop throw degrades the image quality by asymmetric smearing of the point-spread function at a level of 2″ per 1′ of chop amplitude. The resulting image degradation at the long wavelengths (31.5 and 34.8 μm) is quite modest, but at short wavelengths it becomes noticeable for unresolved point sources. No image dithering was employed. After postprocessing, the image pixel is 0.″768. Data reduction was done at the SOFIA Science Center (see Herter et al. 2013, for a thorough description of data acquisition and reduction for FORCAST observations). We use the processed, flux-calibrated (Level 3)

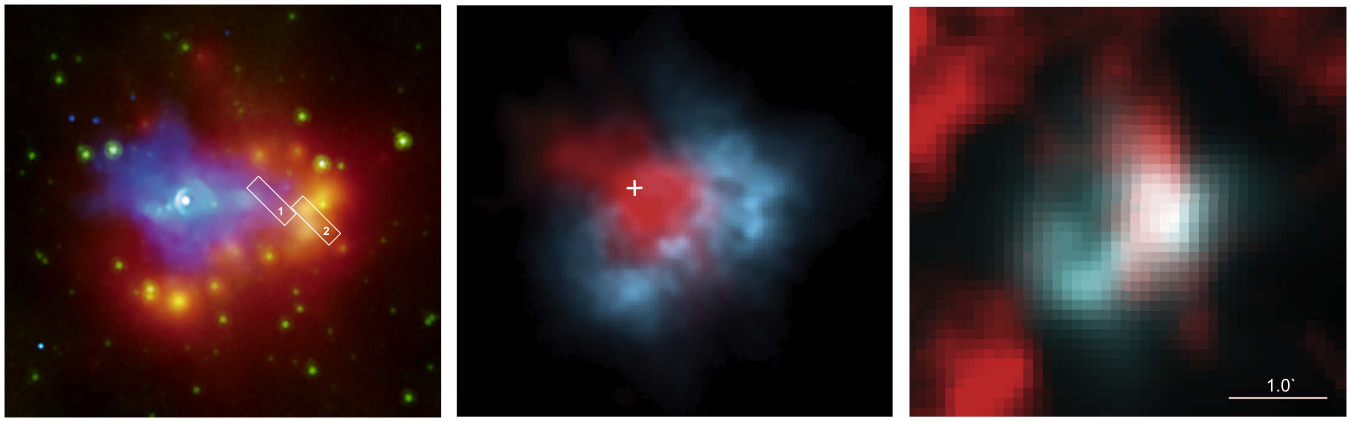

Figure 1. Left: a three-color composite image of G54.1+0.3 with the *Spitzer* 8.0 and 24 μm images in green and red, and the *Chandra* X-ray 0.3–10 keV image in blue (NASA/CXC/SAO/Temim et al. 2010). The PWN seen in X-rays is surrounded by an IR shell with a radius of 1.′3 that emits strongly at 24 μm. A dozen point sources emitting at both 8 and 24 μm are seen in yellow. The white boxes represent the positions of the high-resolution *Spitzer* IRS slits (Temim et al. 2010), with their corresponding line-subtracted spectra shown in Figure 3. Middle: a two-color image showing the 4.8 GHz VLA radio synchrotron emission from the PWN in red and *Herschel* PACS 100 μm infrared emission in cyan. The location of the pulsar is marked by the white plus symbol. Right: *Herschel* SPIRE 250 μm image of the IR shell in red and PACS 70 μm image in teal, convolved to match the 250 μm resolution. The overlay clearly shows the different morphologies of the 70 and 250 μm emission.

images obtained from the raw (Level 1) observations of G54.1+0.3 using the standard FORCAST processing pipeline. The total exposure times are 1625, 1750, 1875, and 1670 s in F197, F253, F315, and F348 filters, respectively. The calibration uncertainty for each band is assumed to be ~20% (Herter et al. 2013). The measured flux of the 25.3 μm image in particular is significantly lower than the measured MIPS 24 μm flux. We suspect that this observation was not sensitive to the fainter extended emission due to the poor throughput of the FORCAST 25.3 μm filter. The lack of faint extended emission is also evident in the FORCAST 25.3 μm image shown in Figure 2. Due to the unreliable flux estimate for the extended emission, we exclude the 25.3 μm SOFIA data point from our analysis and fitting of the IR SED.

2.4. AKARI Image

In our analysis, we also included the *AKARI* Infrared Camera (IRC) 15 μm image of G54.1+0.3 taken on 2007 April 17 (ID: 1401070 001), which has an angular resolution of 5.″7 and was processed with standard pipeline processing. The image was previously presented by Koo et al. (2008).

3. General Morphology

The individual IR images of G54.1+0.3 from 15 to 500 μm are shown in Figure 2, while the morphological comparison of X-ray, radio, and IR wavelengths is shown in the color images of Figure 1. The left panel of Figure 1 shows the three-color image, with the *Chandra* X-ray emission in blue, and *Spitzer* 8 and 24 μm emission in green and red. The X-ray image clearly shows the location of the pulsar (white point source), surrounded by a PWN with a well-defined torus structure (Lu et al. 2002; Temim et al. 2010). There is a jet extending from the pulsar directly toward the west. The 8 μm emission in green primarily shows emission from stellar sources. The 24 μm image shows that the PWN is surrounded by a shell of IR emission, approximately 1.′3 in radius. The dozen point sources that appear yellow in the image also have strong 24 μm fluxes. This is more clearly seen in the individual 24 μm image in Figure 2. The sources appear to be embedded in the diffuse IR emission and arranged in a ring-like structure.

The middle panel of Figure 1 shows the PWN's 4.8 GHz radio emission from the Very Large Array (VLA) in red (Velusamy & Becker 1988), and *Herschel* PACS 100 μm emission in cyan. The location of the pulsar is marked by the white plus symbol. The PWN has a similar spatial extent at radio and X-ray wavelengths. The radio nebula fills the cavity of the shell that is traced by the 100 μm emission and appears to have expanded into this material. The complementary morphology of the radio and IR emission confirms the association and possible interaction between the PWN and the IR shell.

The 15 and 24 μm images show point-like emission that coincides with the stellar sources observed at 8 μm (see Figure 2). In the higher resolution SOFIA images, these sources appear to be somewhat more extended. While the 31.5–100 μm images do show some structure and regions of enhanced emission, there is no clear evidence for point-like emission. At 160 μm and above, the shell emission appears more uniform, partly due to the lower resolution at these wavelengths. While a full shell is still apparent in the 160 and 250 μm images, the emission at 350 and 500 μm arises primarily from a more localized region in the western part of the shell. This may suggest either that there is a higher fraction of colder dust present in this region of the shell, leading to a higher flux density at 500 μm, or that there is more mass, and therefore higher emission, concentrated in the western region. The shell morphology in the mid- and far-IR appears to be different. The emission at 70 μm and even at 100 μm appears more circular, while the shell structure at 250 μm appears more elongated in the north/south direction. This is most apparent in the two-color image shown in the third panel of Figure 1, in which the 70 μm image shown in teal has been convolved to the resolution of the 250 μm image shown in red. The 160 μm emission in Figure 2 seems to be a blend of these two morphologies. In later sections, we will show that the emission in the far-IR either arises from a dust component distinct from the one producing the mid-IR emission or is associated with background emission.

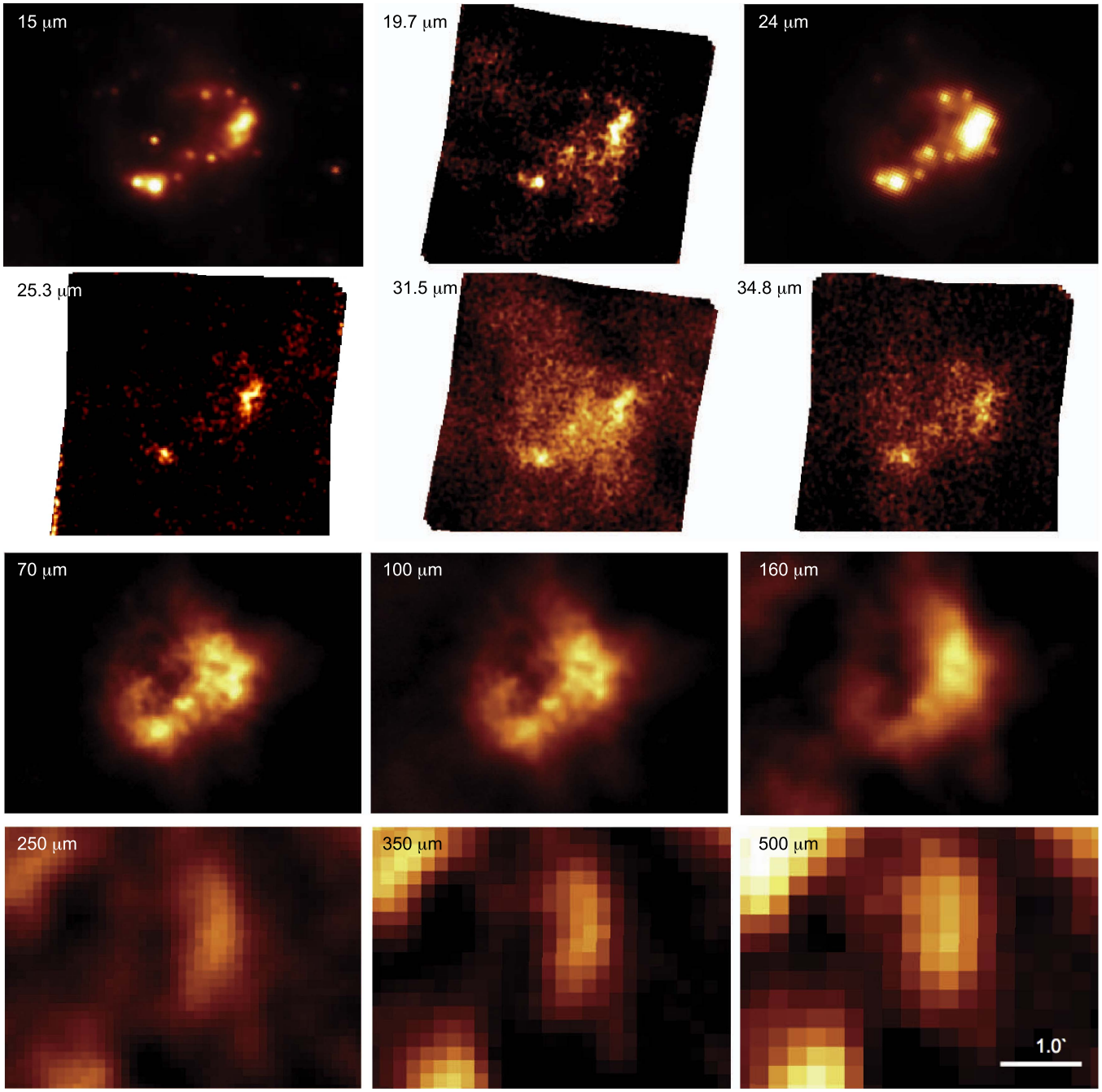

Figure 2. Imaging observations of the infrared shell in G54.1+0.3, including the *AKARI* 15 μm, SOFIA 19.7, 25.3, 31.5, and 34.8 μm, *Spitzer* MIPS 24 μm (Temim et al. 2010), *Herschel* PACS 70, 100, and 160 μm, and *Herschel* SPIRE 250, 350, and 500 μm images. All images are shown on a linear color scale. The integrated background-subtracted flux densities of G54.1+0.3 are listed in Table 1.

4. Origin of the IR Shell

The study of the *Spitzer* IR imaging and spectroscopy of the shell in G54.1+0.3 concluded that the emission most likely arises from newly formed dust in the SN ejecta (Temim et al. 2010). In this scenario, the IR-emitting material is the inner SN ejecta that the PWN is expanding into and that has not yet been reached by the SNR reverse shock. In addition to the complementary morphologies of the PWN and the shell that suggest that they are interacting, modeling of the observed IR line intensities from the shell implies that the PWN is driving a 25–30 km s^{-1} shock into the ejecta. In one particular location (coinciding with Region 2 in Figure 1), the measured gas density is as high as 500–1300 cm^{-3}. This region coincides with a brightness peak in the MIPS 24 μm image and may represent ejecta material that has been compressed by the shock driven by the pulsar's jet (Temim et al. 2010). Another piece of evidence that suggests that the shell material is composed of SN ejecta is the composition of the dust itself (see Section 6.1).

Temim et al. (2010) argued that the IR excess in the point sources in the *Spitzer* 24 μm image (see Figures 1 and 2) is not stellar in origin, but that the emission instead arises from ejecta dust that is being radiatively heated by early-type stars belonging to a stellar cluster in which the SN exploded. The stars heat the dust in their immediate vicinity to higher

temperatures, giving rise to a mid-IR excess that appears point-like due to the limited spatial resolution. This scenario is consistent with the morphology of the images in Figure 2, in which we see that the regions with enhanced brightness in the long-wavelength SOFIA and the MIPS 70 μm images and longward do not appear point-like, but are instead more extended. Kim et al. (2013) classified the spectral type of each star in the shell and concluded that they are indeed late O- and early B-type stars with no evidence for any emission lines that are typically associated with Herbig Ae/Be stars. This provides further evidence that the 24 μm point-like emission is not intrinsic to the stars.

The evidence outlined above strongly suggests that the IR shell is not circumstellar in origin and that the mid-IR point sources are not YSOs. An additional argument against a circumstellar origin is the lack of any X-ray thermal emission that would results from the interaction of the SN blast wave with the surrounding dense material. Additionally, a reverse shock would have formed as the SN blast wave encountered the cloud and significantly disrupted the PWN. However, the well-defined torus and jet structures and the modeling of the PWN evolution (Gelfand et al. 2015) strongly suggest that this has not occurred and that the material that we observe in the shell arises from inner SN ejecta.

The G54.1+0.3 system is analogous to the Crab Nebula, which also consists of a PWN expanding into and radiatively heating SN ejecta and dust (e.g., Hester 2008). However, in the case of G54.1+0.3, the stars that are part of the cluster in which the progenitor was born serve as the primary heating sources for the SN-condensed dust as it blows past them. We note that additional ejecta material may be present beyond the radius of the observed IR shell, but remain undetected due to its low temperature.

5. Analysis of the Dust Emission

5.1. Extraction of Source Fluxes

The source fluxes for the entire IR shell in G54.1+0.3 were measured from the *AKARI*, SOFIA, *Spitzer* MIPS 24 μm, and *Herschel* PACS and SPIRE images that are shown in Figure 2. The SOFIA FORCAST fluxes were extracted from the images using a circular aperture with a radius of 1.′0, centered on the IR shell. Since the observations were performed using the chop/nod technique, the background was already removed from the images. The *AKARI*, *Spitzer*, and *Herschel* fluxes were extracted using an aperture around the IR shell, approximately a circle with a ∼1.′5 radius, and a 4.′1 × 4.′5 rectangular region for the background, centered on the shell and excluding the source extraction region. We used the average value in the rectangular region as the background flux, and the standard deviation of the pixel-to-pixel fluxes within the region as the background uncertainty. Significant spatial variations in the brightness of the background are evident in the 160–500 μm images shown in Figure 2. In calculating the average background in the SPIRE 250–500 μm images, we masked the brightest cores of the surrounding clouds. The overall uncertainties in the measured flux densities longward of 100 μm are dominated by background confusion. The foreground/background stellar sources that appear in the 15 μm *AKARI* image, but not at 24 μm, were excluded from the flux measurement.

Table 1
Observed Infrared Flux Densities

Instrument	Wavelength (μm)	Flux Density (Jy)	Extinction Correction
AKARI IRC	15.6	2.6 ± 0.26	1.38
SOFIA FORCAST	19.7	11.9 ± 2.4	1.38
Spitzer MIPS	24.0	23.1 ± 2.1	1.24
SOFIA FORCAST	25.3	12.7 ± 2.5	1.13
SOFIA FORCAST	31.5	42.5 ± 8.5	1.12
SOFIA FORCAST	34.8	41.7 ± 8.3	1.11
Herschel PACS	70.0	87.9 ± 11.4	…
Herschel PACS	100	68.8 ± 13.4	…
Herschel PACS	160	29.0 ± 14.9	…
Herschel SPIRE	250	6.9 ± 5.2	…
Herschel SPIRE	350	1.6 ± 2.8	…
Herschel SPIRE	500	0.4 ± 1.1	…

Note. Measured background-subtracted infrared flux densities for the G54.1 +0.3 shell before extinction correction. The listed extinction correction factors based on Xue et al. (2016) were used in the SED fitting. See Section 2.3 for more on the discrepancy between the measured MIPS 24 μm and FORCAST 25 μm flux densities.

The IR flux densities for the G54.1+0.3 shell are listed in Table 1. We applied an extinction correction to the 15.0–34.8 μm flux densities using the mid-IR interstellar extinction law derived by Xue et al. (2016) from the SDSS-III/APOGEE spectroscopic survey. For the bands that were not explicitly calculated in Xue et al. (2016), we used the average of the Wang et al. (2015) and the Weingartner & Draine (2001) $R_V = 5.5$ extinction curves (see Figure 18 of Xue et al. 2016). These two curves diverge only for our 15 and 19 μm data points. In deriving the corrections, we assume $A_V = 7.3$ (Kim et al. 2013), leading to $A_K = 0.82$. The final extinction correction factors that were used in the SED fitting are listed in Table 1.

5.2. Fitting of the IRS Spectra

In Figure 3, we show the line-subtracted continuum emission at the two IRS positions shown in Figure 1. The prominent emission feature at ∼21 μm has been attributed to $Mg_{0.7}SiO_{2.7}$ dust grains (Jäger et al. 2003) and used by Arendt et al. (2014) to fit the dust continuum in Cas A. The mass absorption coefficient that clearly shows this feature is plotted as the purple curve in Figure 4. The spectra in Figure 3 show that the feature is much more prominent at position 2 than position 1. We find that the IRS spectra are well fitted by a hotter dust component of either carbon or silicate grains, plus an $Mg_{0.7}SiO_{2.7}$ dust composition emitting at lower temperature. The hot component has a best-fit temperature of 147 ± 2 K (152 ± 1 K) for carbon grains and 146 ± 1 (133 ± 1) for silicate grains at position 1 (position 2). The best-fit temperatures of the $Mg_{0.7}SiO_{2.7}$ dust are 47 ± 1 K and 58 ± 1 K at positions 1 and 2, respectively, independent of whether the carbon or silicate grains are used to model the hot dust component. The fits indicate that the hot dust component dominates the spectra shortward of 17 μm, while the warm component dominates at longer wavelengths. The difference in the shapes of the mid-IR continua at the two positions appears to be caused by variations in the dust temperature of the warm component and not by variations in the grain composition, with

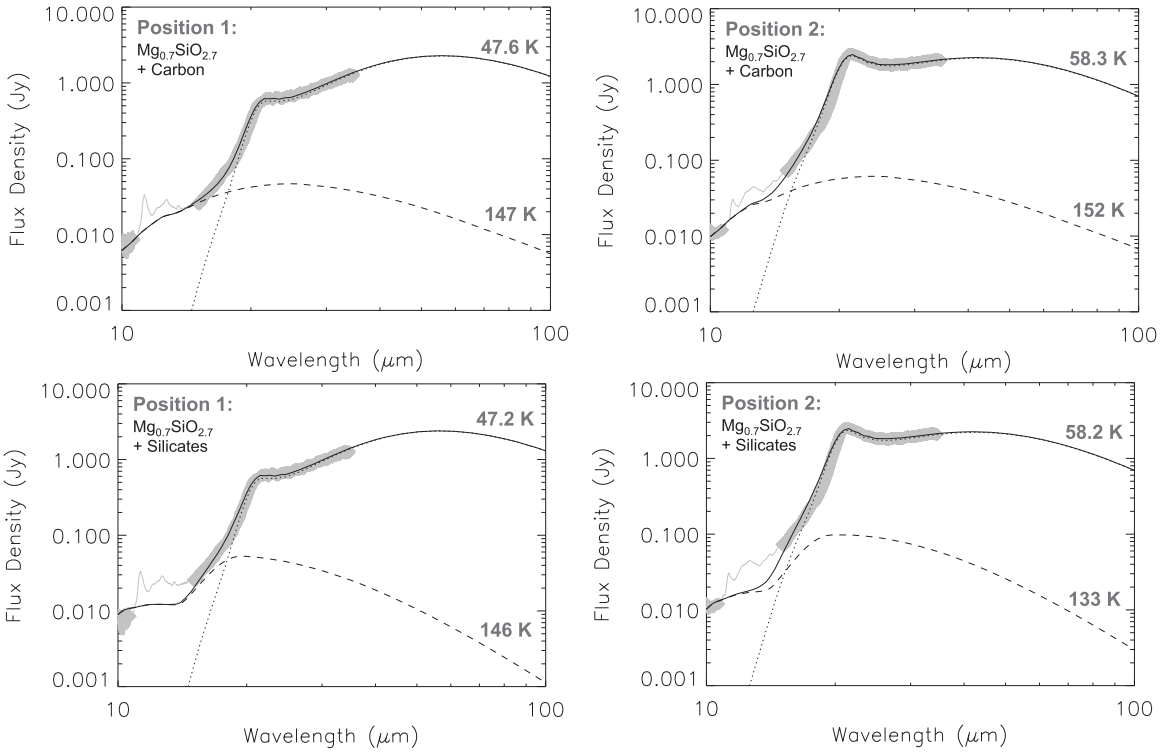

Figure 3. The high-resolution, line-subtracted *Spitzer* IRS spectra from two positions shown in Figure 1 fitted with the $Mg_{0.7}SiO_{2.7}$ dust component shown by the dotted curves, plus a carbon (silicate) component in the top (bottom) row shown as the dashed curves. The gray bands represent the statistical uncertainties in the spectrum. The wavelength region between 11 and 13 μm represented by the gray solid line contains polycyclic aromatic hydrocarbon features and was excluded from the fit. The fits are consistent with a hotter carbon or silicate dust component emitting at a temperature of ~150 K or ~140 K, respectively, plus an $Mg_{0.7}SiO_{2.7}$ component emitting at ~47 K at position 1 and ~58 K at position 2. The different shapes of the IR spectra at the two positions can be explained by variations in the temperature of the $Mg_{0.7}SiO_{2.7}$ dust component.

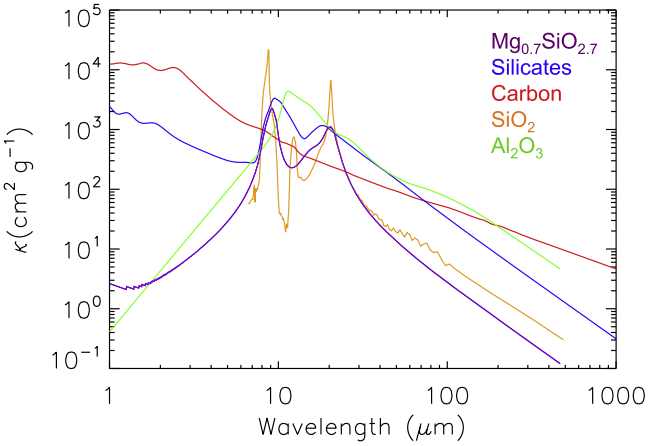

Figure 4. Mass absorption coefficients for the dust species used in the fits, with $Mg_{0.7}SiO_{2.7}$ in purple (Jäger et al. 2003), silicates in blue (Weingartner & Draine 2001), amorphous carbon in red (Rouleau & Martin 1991), SiO_2 in orange (Henning & Mutschke 1997), and Al_2O_3 in green (Begemann et al. 1997).

the less prominent 21 μm feature at position 1 being an effect of a lower dust temperature that peaks at longer wavelengths.

5.3. Global SED Fits

The global SED of the IR shell is shown in Figures 5 and 6, with individual flux density values listed in Table 1. Temim et al. (2010) show that the 21 μm spectral feature is present in all regions covered by the *Spitzer* low-resolution IRS slits, and since the slits span the entire length of the IR shell in the east/west direction, this suggests that the feature is likely present throughout the shell. We also verified that the hot dust component arising from the fits to the IRS high-resolution spectra in Figure 3 is also present in all regions covered by the low-resolution slits. We therefore included the hot dust component from either carbon grains (Figure 5) or silicate grains (Figure 6), as well as a contribution from $Mg_{0.7}SiO_{2.7}$ grains in all of our SED fits. While an additional third component was not statistically significant in the fit, we explored the possibility of its presence using various grain compositions.

As part of our fitting method, we convolved the model spectra with the spectral response of each instrument to derive the expected flux density in each bandpass, applied extinction to each of the values by dividing by the extinction factors in Table 1, and then fitted the resulting values to the observed flux densities. Figures 5 and 6 show the observed flux densities and their uncertainties in red, the best-fit model spectra as the black curves, and the bandpass-integrated and reddened model flux densities in black, with the filter widths indicated by the horizontal black lines.

We first fitted the global SED with two dust components: a hot dust component of either carbon or silicate grains, and a cooler component of $Mg_{0.7}SiO_{2.7}$ grains. We fixed the hot component's temperatures to those found in the spectral fits in Figure 3, 150 K for carbon and 140 K for silicates, while letting their normalizations vary. The resulting best-fit normalization leads to dust masses of $(4.6 \pm 1.2) \times 10^{-5} M_{\odot}$ and $(2.2 \pm 0.5) \times 10^{-5} M_{\odot}$ for carbon and silicate grains, respectively. The resulting relative normalizations of the hot and

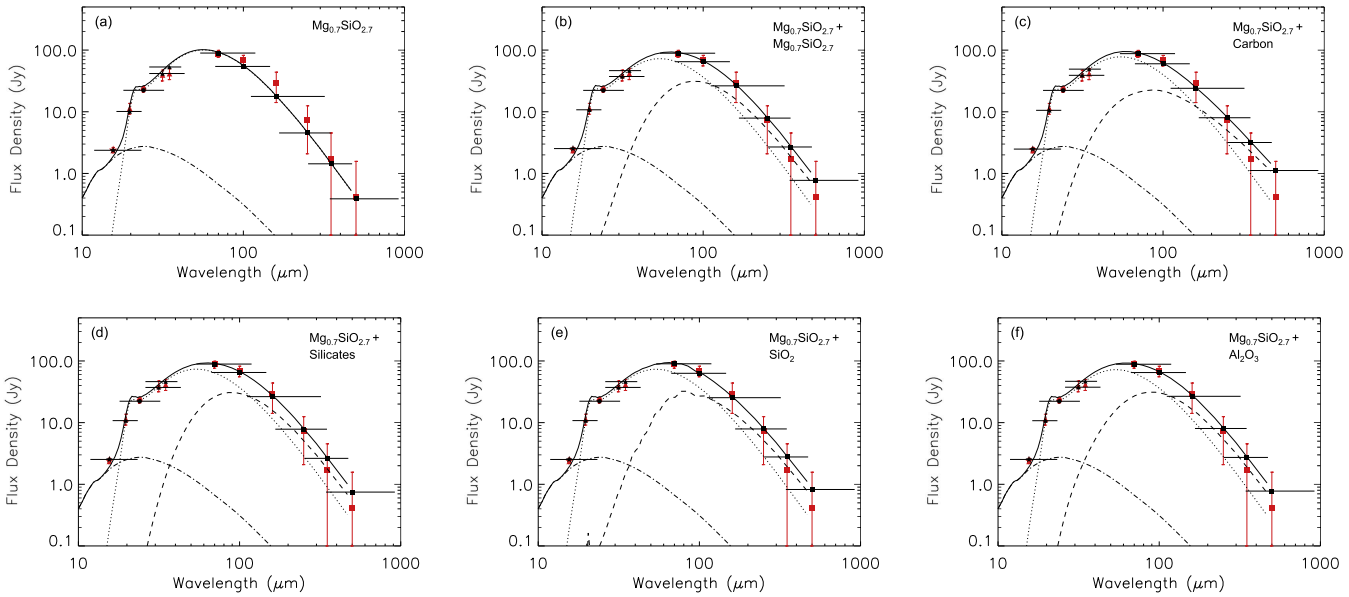

Figure 5. Total SED of the G54.1+0.3 shell, including the *AKARI*, SOFIA, *Spitzer*, and *Herschel* data points as the filled red stars, triangles, circles, and squares, respectively (listed in Table 1). The fits in all panels include a carbon dust component emitting at a temperature of 150 K (dashed–dotted line), as found from the best fit to the IRS spectra in the top panels of Figure 3. The additional component included in panel (a) is a single-temperature $Mg_{0.7}SiO_{2.7}$ dust composition from Jäger et al. (2003). The SEDs in the remaining panels are fitted by two components in addition to the hot carbon dust. The dotted curve in all panels represents the $Mg_{0.7}SiO_{2.7}$ composition while the dashed curves in various panels represent (b) $Mg_{0.7}SiO_{2.7}$, (c) amorphous carbon from Rouleau & Martin (1991), (d) silicates from Weingartner & Draine (2001), (e) SiO_2 from Henning & Mutschke (1997), and (f) Al_2O_3 from Begemann et al. (1997). The black data points represent the model spectra convolved with the filter profiles for each band, and the horizontal black lines represent the total width of the bandpass. In order to fit the observed fluxes, we applied extinction to the model's filter-integrated data points, which explains the slight mismatch between these points and the unabsorbed spectral model. The corresponding dust temperature and masses are listed in Table 2.

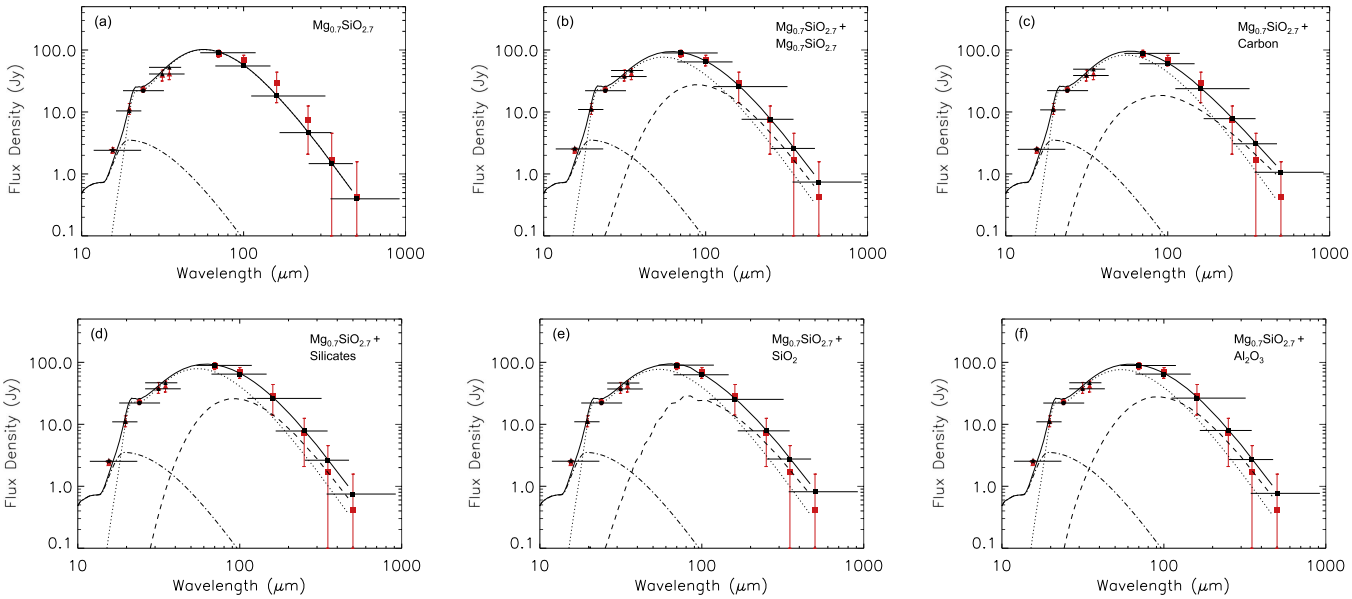

Figure 6. The same as Figure 5, except that here the hot component is composed of silicate grains emitting at a temperature of ∼140 K, as found from the fits to the IRS spectra shown in the bottom panels of Figure 3.

warm components are consistent with those found for the spectral fits.

We then performed fits to the global SED using an additional (third) cold component composed of various grain compositions. In addition to trying an additional cold component of $Mg_{0.7}SiO_{2.7}$ grains (Figure 5(b)), we also tested grains of amorphous carbon (Rouleau & Martin 1991), silicates (Weingartner & Draine 2001), SiO_2 (Henning & Mutschke 1997), and Al_2O_3 (Begemann et al. 1997). The mass absorption coefficients for these grain species are shown in Figure 4, while the best fits to the SED are shown in Figures 5(c)–(f) with carbon as the hot component, and Figures 6(c)–(f) with silicates as the hot component. The best-fit dust temperatures and masses for all models in Figures 5 and 6 are listed in Table 2 and will be discussed in detail in Sections 6.2 and 6.3.

The model of a hot carbon/silicate plus a single warm $Mg_{0.7}SiO_{2.7}$ gives a best-fit temperature of 47 K and a mass of $1.8 \pm 0.3\,M_{\odot}$, assuming a distance of 6.0 kpc. The implausibly large dust mass suggests that the $Mg_{0.7}SiO_{2.7}$ grains are not the

Table 2
Dust Parameters

Comp. 1	Comp. 2	χ^2/dof	T_1 (K)	T_2 (K)	M_1 ($M_\odot$)	M_2 ($M_\odot$)	$M_{\rm tot}\, d_{6.0}^2$ ($M_\odot$)
Hot Dust Component: Carbon							
Including Long-wavelength Residual Emission:							
$Mg_{0.7}SiO_{2.7}$	…	4.6	47 ± 5	…	1.74 ± 0.38	…	1.74 ± 0.38
$Mg_{0.7}SiO_{2.7}$	$Mg_{0.7}SiO_{2.7}$	1.3	49 ± 2	32 ± 9	1.00 ± 0.57	4.31 ± 4.19	5.32 ± 4.44
$Mg_{0.7}SiO_{2.7}$	Carbon	2.5	49 ± 2	44 ± 28	1.16 ± 0.88	0.046 ± 0.046	1.21 ± 0.92
$Mg_{0.7}SiO_{2.7}$	Silicates	1.2	49 ± 2	32 ± 8	1.03 ± 0.50	0.38 ± 0.38	1.41 ± 0.70
$Mg_{0.7}SiO_{2.7}$	SiO_2	1.5	49 ± 2	33 ± 8	1.02 ± 0.51	1.60 ± 1.56	2.63 ± 1.76
$Mg_{0.7}SiO_{2.7}$	Al_2O_3	1.4	49 ± 2	38 ± 14	1.00 ± 0.66	0.079 ± 0.079	1.08 ± 0.70
Excluding Long-wavelength Residual Emission:							
$Mg_{0.7}SiO_{2.7}$	…	2.0	48 ± 1	…	1.52 ± 0.20	…	1.52 ± 0.20
$Mg_{0.7}SiO_{2.7}$	$Mg_{0.7}SiO_{2.7}$	1.4	49 ± 3	40 ± 32	0.89 ± 2.75	1.23 ± 1.48	2.13 ± 1.78
$Mg_{0.7}SiO_{2.7}$	Carbon	1.79	48 ± 1	44 ± 82	1.33 ± 0.96	0.015 ± 0.049	1.34 ± 0.99
$Mg_{0.7}SiO_{2.7}$	Silicates	1.4	49 ± 1	39 ± 14	0.99 ± 0.65	0.10 ± 0.11	1.09 ± 0.69
$Mg_{0.7}SiO_{2.7}$	SiO_2	0.94	49 ± 2	46 ± 4	0.90 ± 0.48	0.33 ± 0.33	1.22 ± 0.22
$Mg_{0.7}SiO_{2.7}$	Al_2O_3	1.6	49 ± 2	43 ± 29	1.12 ± 0.87	0.03 ± 0.03	1.14 ± 0.88
Hot Dust Component: Silicates							
Including Long-wavelength Residual Emission:							
$Mg_{0.7}SiO_{2.7}$	…	4.1	47 ± 1	…	1.80 ± 0.25	…	1.80 ± 0.25
$Mg_{0.7}SiO_{2.7}$	$Mg_{0.7}SiO_{2.7}$	1.4	49 ± 2	31 ± 9	1.13 ± 0.62	4.21 ± 4.21	5.34 ± 4.71
$Mg_{0.7}SiO_{2.7}$	Carbon	2.4	48 ± 1	43 ± 28	1.32 ± 0.81	0.045 ± 0.045	1.36 ± 0.85
$Mg_{0.7}SiO_{2.7}$	Silicates	1.3	48 ± 2	31 ± 9	1.14 ± 0.55	0.38 ± 0.38	1.52 ± 0.76
$Mg_{0.7}SiO_{2.7}$	SiO_2	1.5	48 ± 2	32 ± 9	1.14 ± 0.56	1.57 ± 1.57	2.71 ± 1.86
$Mg_{0.7}SiO_{2.7}$	Al_2O_3	1.4	49 ± 2	37 ± 15	1.13 ± 0.71	0.077 ± 0.077	1.20 ± 0.76
Excluding Long-wavelength Residual Emission:							
$Mg_{0.7}SiO_{2.7}$	…	1.7	47 ± 1	…	1.55 ± 0.20	…	1.55 ± 0.20
$Mg_{0.7}SiO_{2.7}$	$Mg_{0.7}SiO_{2.7}$	1.2	50 ± 6	42 ± 43	0.66 ± 6.24	1.31 ± 5.10	1.98 ± 1.32
$Mg_{0.7}SiO_{2.7}$	Carbon	1.5	48 ± 1	45 ± 91	1.37 ± 1.02	0.014 ± 0.048	1.38 ± 1.06
$Mg_{0.7}SiO_{2.7}$	Silicates	1.1	49 ± 1	39 ± 14	1.01 ± 0.66	0.11 ± 0.11	1.12 ± 0.70
$Mg_{0.7}SiO_{2.7}$	SiO_2	0.8	49 ± 1	45 ± 5	0.95 ± 0.44	0.34 ± 0.34	1.29 ± 0.26
$Mg_{0.7}SiO_{2.7}$	Al_2O_3	1.3	49 ± 1	41 ± 37	1.23 ± 0.86	0.024 ± 0.050	1.26 ± 0.88

Note. Temperatures and masses for fits of the individual warm and cold dust components to the global SED. The contributions of the hot carbon (top half of table) and silicate (bottom half of table) components were kept constant for all fits. The dust masses were calculated based on an assumed distance of 6.0 kpc. The table also lists the best-fit model parameters for the global SED fits after the subtraction of the long-wavelength residual emission that may arise from the background (see Section 5.4).

sole contributors to the mid-IR SED and that other grain compositions are likely also present. The addition of another composition resulted in a lower χ^2 for all models, with carbon grains providing a somewhat higher χ^2 than the others due to their flatter slope in emissivity at longer wavelengths (see Figure 4). The best-fit temperature of the primary $Mg_{0.7}SiO_{2.7}$ dust component is ∼47–49 K for all model combinations. The temperature and mass of the secondary dust composition are not well constrained, and this produces very large uncertainties in the relative masses of the different grain compositions as well as in the total dust mass in the shell.

The relative flux densities of the best-fit models plotted in Figures 5 and 6 appear to be consistent with the observed morphologies in Figure 2. For instance, as mentioned in Section 3, the morphology at 100 μm and below is different than the observed structure at 250 μm. The best fits to the global SED show that the emission up to 100 μm is dominated by the warm dust component, while the colder dust component that may have a different spatial morphology dominates at 250 μm and above. In the 160 μm band, the warm and cold components have comparable contributions. In later sections, we will explore the possibility that the emission at 250 μm and above actually arises from a background cloud.

5.4. Spatially Resolved Fits: Dust Mass and Temperature Maps

In order to explore the spatial variations in the dust temperature and mass of the shell, we fitted the SEDs of individual pixels across the shell using a single dust component of $Mg_{0.7}SiO_{2.7}$ grains. In order to preserve the spatial resolution, minimize the effects of the background confusion, and also to model only wavelengths that appear to have similar morphologies, we used only the 15–100 μm images in our fits. The SOFIA images were also excluded due to the poor sensitivity to the fainter emission in the shell. The images were all convolved to the PACS 160 μm resolution using the convolution kernels of Aniano et al. (2011), resulting in a pixel size of 3.″2. The SED fits provided a temperature and

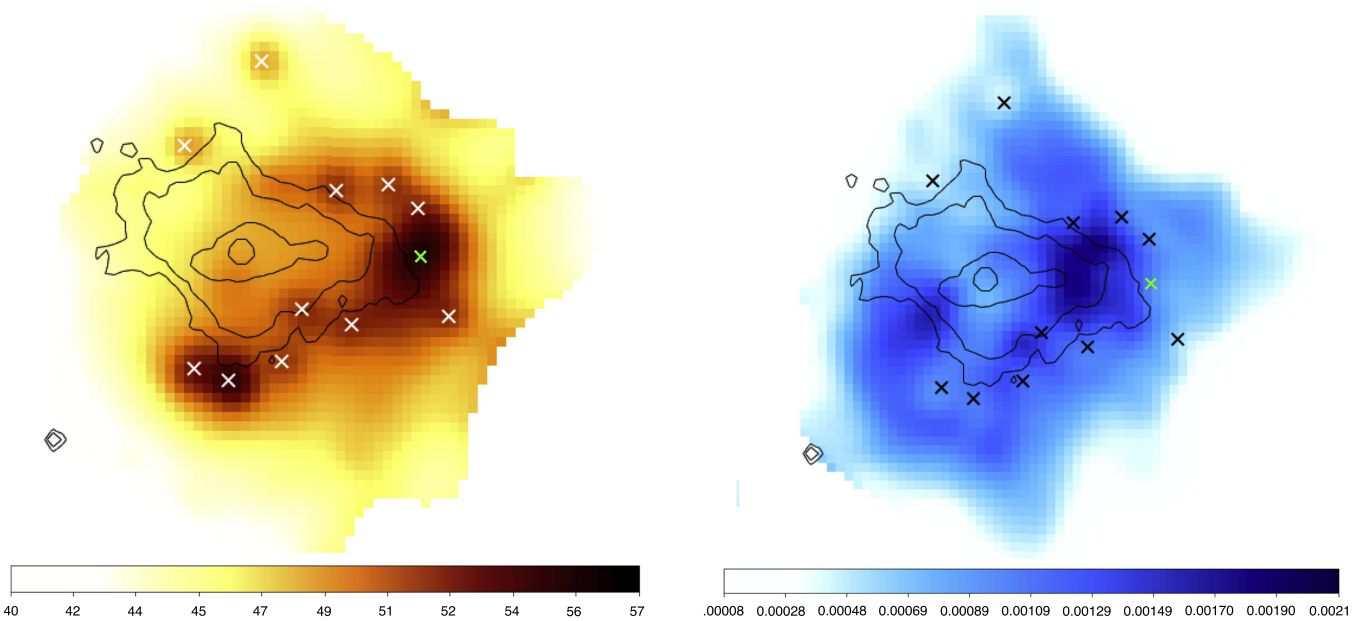

Figure 7. Maps of temperature in units of kelvin (left) and the dust mass surface density in units of $M_{\odot}$/pixel, where the pixel size is $3\farcs2$ (right), resulting from the fits to the individual pixels' 15–100 μm SEDs, using the $Mg_{0.7}SiO_{2.7}$ dust composition. The "×" symbols represent the location of the O and B stars (those identified by Koo et al. (2008) in white and those by Morris et al. (2010) in green), while the black contours represent the X-ray PWN. The temperature map clearly shows that the dust temperature peaks around the stars, implying that these O and B stars are the primary heating sources for the dust. The distribution of the dust mass surface density does not show correlation with the stellar sources, but instead reveals a region of enhanced density at the western boundary of the PWN.

corresponding dust mass for each pixel. These maps are shown in Figure 7, with the left panel showing the temperature and the right panel showing the dust mass surface density. The black contours represent the *Chandra* X-ray emission from the PWN seen in Figure 1, while the "×" symbols represent the locations of the stars identified by Koo et al. (2008) and Morris et al. (2010).

The temperature in the shell varies from 42 to 57 K with an average temperature and standard deviation of 46 ± 4 K. The sum of the individual pixels in the map of dust mass surface density leads to a total dust mass of $1.8 \pm 0.3\,M_{\odot}$, consistent with the mass derived from fitting the integrated SED of the shell using only $Mg_{0.7}SiO_{2.7}$ grains (see Table 2). The maps of dust mass and temperature are consistent with the physical scenario proposed by Temim et al. (2010) in which the stellar sources heat the surrounding SN-condensed dust, since the temperature clearly peaks at the locations of the stellar sources, while the dust mass surface density shows no such correlation. The map of dust mass surface density does show a slight deficiency in dust mass at the locations of the brightest stellar sources. The most likely explanation for this deficiency is that the temperature at the locations of the stars was slightly overestimated due to the inclusion of 15 μm data that have a significant contribution from hot dust.

In order to determine how well the single-component spatial fits match the global SED, we compared the observed and model-predicted flux densities of the shell at all observed wavebands. While the 19–70 μm data are well represented by the model, the 15 μm flux is underestimated by ∼35%. The model also underestimates the observed emission at 100, 160, 250, 350, and 500 μm, by 28%, 44%, 43%, 23%, and 16%, respectively. In order to investigate the nature of the excess emission above the best-fit spatial model, we used the maps of dust mass and temperature in Figure 7 to produce model-predicted flux density images at 15, 24, 70, 100, and 160 μm, and then divided the observed images by these maps to produce ratio maps. The ratio maps are shown in Figure 8, all using the same linear scale (0.8–3.3) and color scheme. The blue color indicates a ratio of ∼1, where the model most closely matches the observation, while the values above unity show the spatial distribution of the emission excess that was not well predicted by the model. The 24 and 70 μm emission is clearly well described by the model across the entire shell, while there is a clear excess at 15, 100, and 160 μm.

The spatial distribution of the excess at 15 μm is particularly interesting. It does not correlate at all with the shell morphology at 24 μm, but is instead concentrated along a thin shell on the outskirts of the observed mid-IR shell, as well as at a couple of point sources, one of which is a background source not associated with the SNR. This suggests that the 15 μm excess emission does not belong to the same dust component that emits at 24 μm, but instead may be produced by hot dust grains that have a different spatial distribution or by line emission that could partly contribute to the 15 μm *AKARI* band. One hypothesis is that very small dust grains in the shell are heated to temperatures much higher than the equilibrium temperature because of their lower heat capacity, and that their emission is more pronounced at the outskirts of the cluster, where the radiation field starts to drop off and where the temperature of the larger grains is lower. The presence of this hot component is also supported by the fits to the IRS spectra shown in Figure 3. We note here that the average contribution of the hot dust component in the IRS fits to the 15 μm *AKARI* waveband is ∼35%, the same fraction that is seen in the 15 μm excess above the best spatial fit (first panel of Figure 8).

The ratio maps at 100 and 160 μm show that the morphology of the excess emission resembles the morphology in the far-IR. This is seen more clearly in Figure 9, where we show the observed 160 μm image in panel (a), the spatial model-

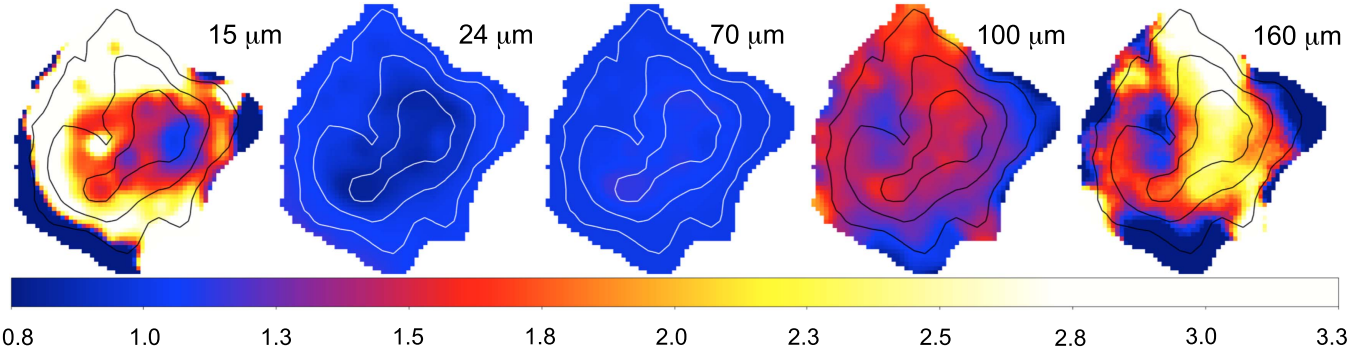

Figure 8. Ratio maps of the background-subtracted *AKARI* 15 μm, MIPS 24 μm, and PACS 70, 100, and 160 μm images and maps of the flux-density at corresponding wavelengths derived from the best-fit dust and temperature maps shown in Figure 7. The contours represent the 70 μm shell emission. A ratio of 1 (blue) indicates that the best-fit spatial model accounts for all of the observed flux, while a higher ratio indicates an observed excess above the best-fit model. The ratio maps provide information about the morphology of the emission excess; the excess at 15 μm has a different morphology than the IR shell observed in the mid-IR, while the excess at 100 and 160 μm resembles the morphology seen at 250 μm and longward, suggesting that it arises from a contribution from a secondary dust component.

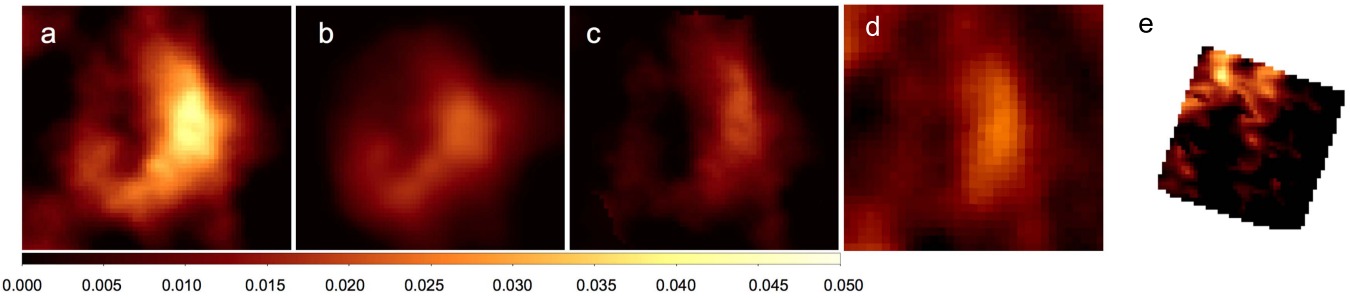

Figure 9. (a) PACS 160 μm image in units of Jy/pixel. (b) Model-predicted 160 μm flux calculated from the mass and temperature maps in Figure 7. (c) The residual 160 μm emission after subtraction of the model-predicted flux. Images in panels (a)–(c) are on the same brightness scale and stretch. (d) 250 μm SPIRE image that shows the same morphology as the residual 160 μm emission in panel (c). (e) Map of the [C II] 157.7 μm line emission that does not spatially correlate with the IR shell, but does show some resemblance to the 15 μm excess emission shown in Figure 8.

predicted 160 μm flux arising from $Mg_{0.7}SiO_{2.7}$ in panel (b), the residual between the observed image and the fitted model in panel (c), and the 250 μm observed image in panel (d). For comparison, we also show a map of the [C II] 157.7 μm line emission from the PACS spectral observations in Figure 9(e), which does not seem to correlate with the 160 μm dust emission, but instead shows a spatial distribution more similar to the morphology of the 15 μm excess in Figure 8. The residual map in Figure 9(c) clearly shows that the excess emission at 160 μm closely resembles the morphology at 250 μm, suggesting that the 100 and 160 μm excess above the $Mg_{0.7}SiO_{2.7}$ spatial model arises either from a distinct dust component that dominates the emission at longer wavelengths or from background emission not associated with the SNR.

In Section 5.3, we explored the possibility that an additional dust component with a different composition contributes to the global SED of the shell and dominates the emission at wavelengths longer than 100 μm. The best-fit parameters for the models that include this secondary component are listed in Table 2. Another possibility is that the emission at long wavelengths actually originates from a background cloud, since the morphology at wavelengths longer than 160 μm differs from the morphology at shorter wavelengths. If we assume that the emission at 24–70 μm is dominated by a single dust component of $Mg_{0.7}SiO_{2.7}$, as was assumed in the spatial fit, we can then test whether the level of residual emission at longer wavelengths is consistent with the surrounding background. In Figure 10, we show a scatter plot of the 100 versus 160 μm flux densities for the observed emission in the shell, the best-fit spatial model for a single component of $Mg_{0.7}SiO_{2.7}$ grains, the residual emission after the subtraction of the spatial model, and finally, the background emission in an annulus surrounding the source. The gray lines represent the 160/100 μm ratios for various temperatures of $Mg_{0.7}SiO_{2.7}$ grains. As can be seen from the plot, the best-fit spatial model is composed of grains emitting in a narrow temperature range between 45 and 55 K (also seen in the left panel of Figure 7), while the long-wavelength residual is seen to have the same properties as surrounding background emission.

In this scenario, the $Mg_{0.7}SiO_{2.7}$ grains with a temperature and mass distribution shown in Figure 7 dominate the emission from 15 to 100 μm, while residual background emission significantly contributes to the 160 μm flux and dominates at the far-IR SPIRE wavelengths. We therefore performed additional fits to the global SED, assuming that the residual long-wavelength emission arises from the background. We used the same compositions as in Section 5.3, but subtracted the residual long-wavelength emission from the integrated flux densities. Since the fit, by definition, is well described by a single component of warm $Mg_{0.7}SiO_{2.7}$ grains (in addition to the hot component derived from the spectral fits), a third component is not statistically significant. However, adding this component allowed us to test whether an addition of grains of a different composition affects the best-fit dust parameters. The results of the fits are included in Table 2, in the subsections indicating that the long-wavelength residual emission has been excluded, and will be discussed in Sections 6.2 and 6.3.

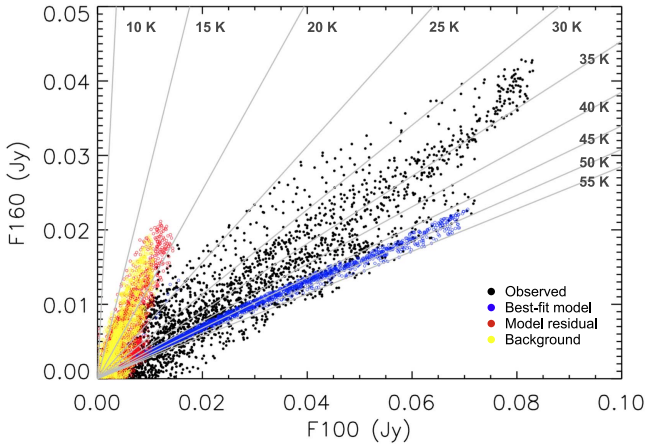

Figure 10. Scatter plot of the 100 μm flux density vs. the 160 μm flux density for the observed emission in the IR shell (black), the best-fit spatial model using $Mg_{0.7}SiO_{2.7}$ grains (blue), the observed minus model residual emission (red), and the flux densities from an annular background region around the source (yellow). The solid gray lines represent the 160/100 μm flux density ratios for various temperatures. The best-fit spatial model produces a temperature between 45 and 55 K, while the long-wavelength residual has the same characteristics as the surrounding background.

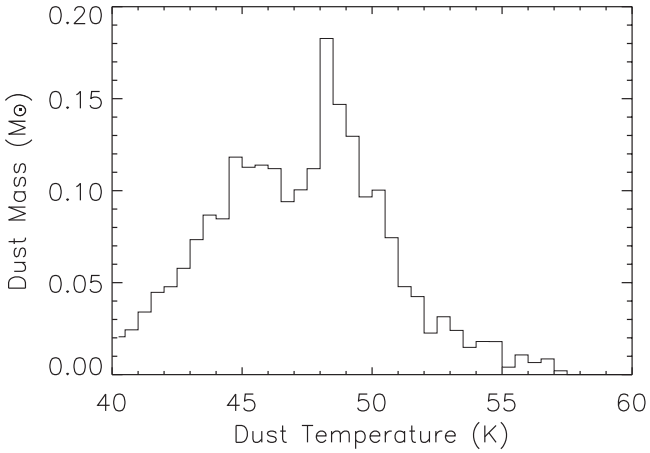

Figure 11. Distribution of dust mass as a function of temperature resulting from the best-fit maps shown in Figure 7. The plot shows that most of the dust mass emits in a narrow temperature range between 45 and 51 K. The peak at a temperature of ~49 K originates from the enhanced region of surface mass density that is evident in the right panel of Figure 7.

6. Dust Properties

6.1. Composition

The prominent spectral feature that is observed at 21 μm has the same spectral profile as the feature observed in the spectrum of the SN-condensed dust in Cas A (Arendt et al. 1999; Ennis et al. 2006). As far as we know, Cas A and G54.1+0.3 are the only two sources whose spectra exhibit a feature of this particular shape. Arendt et al. (2014) attributed the feature to $Mg_{0.7}SiO_{2.7}$ grains, characterized by an MgO to SiO_2 ratio of 0.7. Out of 60 different grain compositions that they tested, this species is the only one that has a 21 μm spectral feature that fits the width and shape of the feature observed in Cas A. As discussed in Section 5.2, we confirmed that the same grain species can fit the *Spitzer* high-resolution spectra of G54.1+0.3 that are shown in Figure 3. Since the 21 μm feature is present throughout the low-resolution IRS slits that run across the IR shell (Temim et al. 2010), we used the $Mg_{0.7}SiO_{2.7}$ grains as the primary component in all our fits, but also included other common grain compositions predicted by dust condensation models in Type IIP SNe for possible secondary components. For example, the models of Kozasa et al. (2009) and Sarangi & Cherchneff (2015) predict that 80%–100% of the SN-condensed dust in Type IIP explosions of $\sim 20\,M_{\odot}$ progenitors is made up of carbon, alumina, and some form of magnesium silicate grains. The mass absorption coefficients of the grain species used in our fits are shown in Figure 4, and they include amorphous carbon, silicates, SiO_2, and Al_2O_3. Another common dust composition predicted by Kozasa et al. (2009) is MgO, but our fits disqualify a major contribution from this species because of its spectral feature at ~100 μm that does not appear in the SED of the shell.

The best fits in Figure 5 and Table 2 indicate that if the $Mg_{0.7}SiO_{2.7}$ grains are indeed responsible for producing the feature and account for a significant fraction of the observed emission at mid-IR wavelengths, then they are a major component of the total dust mass in the shell. Any additional component is equally well fitted by the other grain species we tested (see Table 2), with the exception of a carbon component, which results in a somewhat larger χ^2. This is due to the fact that the absorption coefficient for carbon grains (see Figure 4) produces a somewhat flatter slope at longer wavelengths than indicated by the SPIRE data.

6.2. Temperature

The map in Figure 7 shows the temperature distribution of the $Mg_{0.7}SiO_{2.7}$ grains. Since the grains at any given location will likely have a distribution of sizes, the temperature for any given pixel should be thought of as the average temperature for that location. The temperature of the dust in the shell ranges from 42 to 57 K, with an average temperature and standard deviation of 46 $\pm$ 4 K. The plot in Figure 11 shows the mass–temperature distribution in the shell, and indicates that most of the mass is actually emitting in a narrow temperature range of 43–52 K. This explains why the mass of the single-temperature warm component fit in Table 2 is similar to that found from the spatially resolved fit, unlike what would be expected for a very wide dust temperature distribution in the shell (Temim & Dwek 2013).

The left panel of Figure 7 clearly shows that the temperature peaks at the location of the stars that are embedded in the shell, confirming that the stars are the primary heating sources for the surrounding dust. In order to verify that this is plausible, we compared the total luminosity of the 11 O and B stars in the shell analyzed by Kim et al. (2013) to the total luminosity of the IR SED seen in Figure 5. Based on the spectral classification of the stars, we assume a luminosity of $25{,}000\,L_{\odot}$ for each star. We calculate the IR luminosity of the shell to be $\sim 9500\,L_{\odot}$, which is only a small fraction of the total luminosity of the stars, approximately 3.5%. We note that there may be additional stars present inside the volume of the shell for which near-IR spectroscopy was not obtained by these authors. In particular, the bright extended region in the left panel of Figure 1 that coincides with position 2 of the IRS slit and also shows up as a hot region in the dust temperature map in Figure 7 is likely heated by an early-type star identified by Morris et al. (2010), but not studied by Kim et al. (2013). The location of this star is marked by the green "×" in Figure 7. This region also has a higher gas density that is likely produced by the compression of the ejecta material by the pulsar's jet

Table 3
Dust Masses Allowed by Nucleosynthetic Yields

M_* ($M_\odot$)	M_i ($M_\odot$)					N_{Mg}/N_{Si}	M_d ($M_\odot$)			
	C	O	Mg	Al	Si		$Mg_{0.7}SiO_{2.7}$	$MgO+SiO_2$	Al_2O_3	$Mg_{0.7}SiO_{2.7}$ + C
Woosley & Heger (2007):										
13.0	0.0949	0.5712	0.0505	0.0041	0.0707	0.83	0.222	0.234	0.008	0.316
14.0	0.1154	0.7229	0.0579	0.0046	0.0713	0.94	0.223	0.248	0.009	0.339
15.0	0.1336	0.8380	0.0525	0.0041	0.0742	0.82	0.232	0.245	0.008	0.366
16.0	0.1577	0.9371	0.0529	0.0041	0.0490	1.25	0.154	0.192	0.008	0.311
17.0	0.1768	1.3604	0.0826	0.0064	0.1715	0.56	0.427	0.502	0.012	0.604
18.0	0.1960	1.6358	0.1496	0.0137	0.1110	1.56	0.348	0.483	0.026	0.544
19.0	0.2077	1.8711	0.0985	0.0093	0.1358	0.84	0.426	0.452	0.018	0.633
20.0	0.2336	1.9604	0.1112	0.0089	0.2178	0.59	0.575	0.648	0.017	0.809
21.0	0.2701	2.5558	0.1536	0.0146	0.1296	1.37	0.406	0.530	0.028	0.676
22.0	0.2591	2.5249	0.1204	0.0117	0.2170	0.64	0.623	0.662	0.022	0.882
23.0	0.2986	2.5480	0.1478	0.0119	0.2556	0.67	0.764	0.789	0.022	1.063
24.0	0.2825	3.0035	0.2442	0.0207	0.2663	1.06	0.834	0.971	0.039	1.117
25.0	0.3629	3.3841	0.2307	0.0204	0.2990	0.89	0.937	1.018	0.039	1.300
26.0	0.3331	3.7727	0.1335	0.0154	0.3686	0.42	0.691	1.007	0.029	1.024
27.0	0.3159	4.0532	0.1674	0.0198	0.2937	0.66	0.866	0.903	0.037	1.182
28.0	0.3793	4.1549	0.2012	0.0229	0.1631	1.43	0.511	0.680	0.043	0.890
29.0	0.3828	4.8632	0.2474	0.0285	0.1788	1.60	0.560	0.789	0.054	0.943
30.0	0.4324	5.1512	0.3411	0.0328	0.1671	2.36	0.524	0.918	0.062	0.956
40.0	0.4501	6.4855	0.3656	0.0396	0.1627	2.60	0.510	0.949	0.075	0.960
60.0	6.1495	6.5599	0.1673	0.0168	0.2096	0.92	0.657	0.723	0.032	6.806
Sukhbold et al. (2016):										
12.7	0.1101	0.3886	0.0341	0.0022	0.0481	0.81	0.151	0.159	0.004	0.261
13.4	0.1177	0.5650	0.0489	0.0039	0.0551	1.03	0.172	0.198	0.007	0.290
13.8	0.1265	0.6189	0.0504	0.0038	0.0600	0.97	0.188	0.211	0.007	0.314
14.3	0.1365	0.7046	0.0563	0.0044	0.0606	1.08	0.190	0.222	0.008	0.326
14.7	0.1493	0.7608	0.0539	0.0041	0.0615	1.01	0.192	0.220	0.008	0.342
15.4	0.1718	0.9740	0.0628	0.0047	0.0825	0.89	0.259	0.279	0.009	0.430
16.2	0.1908	1.1489	0.0705	0.0052	0.0994	0.81	0.312	0.328	0.010	0.503
16.6	0.1973	1.2113	0.0748	0.0054	0.1047	0.82	0.329	0.347	0.010	0.526
17.0	0.2054	1.2862	0.0785	0.0056	0.1102	0.82	0.346	0.364	0.011	0.551
17.5	0.1974	1.5079	0.1216	0.0083	0.0790	1.78	0.247	0.368	0.016	0.445
18.1	0.1959	1.6296	0.1493	0.0136	0.1044	1.67	0.326	0.469	0.026	0.522
19.0	0.2133	1.9239	0.1239	0.0108	0.1426	1.59	0.277	0.508	0.020	0.490
20.1	0.2426	2.1250	0.0956	0.0101	0.3170	0.37	0.495	0.835	0.019	0.737
20.7	0.2278	2.4074	0.1343	0.0132	0.2163	1.53	0.396	0.683	0.025	0.624
21.4	0.2670	2.4646	0.1322	0.0120	0.0954	1.75	0.299	0.420	0.023	0.566
25.4	0.3765	3.5207	0.1051	0.0119	0.4236	0.28	0.540	1.078	0.022	0.917
25.9	0.3518	3.7937	0.1491	0.0179	0.4278	0.40	0.771	1.159	0.034	1.122
26.3	0.4097	3.7250	0.1423	0.0157	0.2861	0.57	0.730	0.845	0.030	1.140
27.2	0.4449	4.0087	0.1661	0.0188	0.2071	0.92	0.650	0.714	0.035	1.095
60.0	0.7750	3.4600	0.1234	0.0131	0.1071	1.31	0.336	0.430	0.025	1.111

Note. M_* represent the mass of the progenitor star. The value M_i represents the total mass of the given atom i (Woosley & Heger 2007; Sukhbold et al. 2016). N_{Mg}/N_{Si} is the ratio of the numbers of Mg to Si atoms in the ejecta. The dust masses M_d represent the maximum masses of dust that can form in the ejecta of a given composition, assuming a 100% condensation efficiency. The amount of $Mg_{0.7}SiO_{2.7}$ is limited by the total number of Mg or Si atoms, depending on whether the Mg/Si number ratio is less than or greater than 0.7. $M_d(MgO+SiO_2)$ is the maximum amount of dust that can form, assuming that all Mg and Si are locked up in MgO and SiO_2 grains. $M_d(Al_2O_3)$ assumes all Al is locked up in dust, and $M_d(Mg_{0.7}SiO_{2.7}$ + C) is the combined mass of the maximum possible $Mg_{0.7}SiO_{2.7}$ and carbon dust yields.

(Temim et al. 2010), but while the jet may contribute to some heating of the dust in this location, the dust temperature distribution and total luminosity imply that the stars are responsible for most of the heating.

The results from the global SED fits in Table 2 show that all model combinations result in $Mg_{0.7}SiO_{2.7}$ grains that are warmer on average than the secondary dust component of a different composition. While a physical dust heating model for the dust in the shell will be explored in a future publication, our preliminary model for heating of dust around a single B0V star (see Temim et al. 2010) confirms that the $Mg_{0.7}SiO_{2.7}$ grains are heated to higher temperatures than carbon or silicate grains of comparable size. It furthermore shows that the typical grain size of the $Mg_{0.7}SiO_{2.7}$ dust would need to be relatively large (of the order of $\sim$1 μm) to achieve the temperatures produced by the best fits in Table 2.

6.3. Mass

The map of dust mass surface density in the right panel of Figure 7 shows that the dust in G54.1+0.3 is fairly uniformly

distributed throughout the shell, with one region of enhancement corresponding to position 1 of Figure 1. The dust mass associated with this enhancement is approximately ∼5% of the total dust mass in the shell. We note that this region does not coincide with the temperature peak at the western edge of the PWN where the gas density enhancement is found by Temim et al. (2010), but instead seems to spatially coincide with the [Si II] peak seen in Figure 11 of Temim et al. (2010). The emission from this region was suggested to arise from ejecta material swept up by the PWN (see Figure 14 of Temim et al. 2010).

The best-fit total dust masses for various combinations of compositions are listed in Table 2. We present the results that assume that the long-wavelength emission originates from the shell, as well as the results that treat this emission as background emission. The models for which the mid-IR emission arises solely from $Mg_{0.7}SiO_{2.7}$ grains produce unreasonably large best-fit dust masses that are inconsistent with nucleosynthetic yields for SN ejecta. This suggests that other grain species with higher emissivities at longer wavelengths are also present in the shell. When a secondary dust composition is included in the models, the best-fit dust masses are somewhat lower, but still higher than what might be expected for SN-condensed dust. For example, for models considering carbon, silicate, or alumina grains as secondary components, the best-fit dust masses range from 1.1 to 1.5 $M_{\odot}$. However, since the temperature and mass of the secondary component are poorly constrained, the uncertainty on the total mass can be as high as $\pm 1\,M_{\odot}$. The lower dust mass limit for the best-fit models in Table 2 (the best-fit value minus the uncertainty) ranges from 0.26 to 1.0 $M_{\odot}$, depending on the chosen composition of the secondary component. These lower limits are achieved when the flux density contribution of the secondary dust component to mid-IR wavelengths is at a maximum, which slightly raises the temperature and decreases the normalization of the primary $Mg_{0.7}SiO_{2.7}$ dust component, effectively decreasing the total dust mass in the shell.

We emphasize that the inferred dust masses are highly dependent on the model that we use to fit the SED. While our choice of grain compositions was motivated by the observed spectral feature and most common dust species arising from dust condensation models, the relative contributions and temperatures of the various dust components will need to be verified by physical dust heating models that properly take into account the radiation field produced by the stellar cluster and a distribution of dust grain sizes and temperatures. For example, a model that included radiative heating of dust grains with a continuous size distribution in the Crab Nebula resulted in a total dust mass that is a factor of two lower than for a two-temperature model that fits the data equally well and uses the same dust grain composition (Temim & Dwek 2013). In future work, it will be important to determine whether the parameter space produced by a heating model will allow for a significantly lower total dust mass in G54.1+0.3. Additional limitations and sources of uncertainty are discussed in Section 6.4.

6.4. Caveats and Limitations

The estimated dust masses in this work are highly dependent on the chosen model parameters and would vary with changes in the source distance and the composition, shape, size distribution, porosity, and clumping of the dust grains. One of the main assumptions that drives the total dust mass is that the 21 μm feature and a significant fraction of the mid-IR continuum in the spectrum of the G54.1+0.3 shell arise from $Mg_{0.7}SiO_{2.7}$ grains. Based on the available optical constants, this grain composition is the only one that reproduces the precise shape of the 21 μm feature (see Arendt et al. 2014). However, there may be other grain compositions with higher emissivities at wavelengths longward of this feature that reproduce it equally well, which would in turn lower the estimated dust mass.

As mentioned in Section 6.3, introducing a wide distribution of grain sizes, and therefore temperatures, may also affect the relative contribution of the various dust species to the global SED and change the derived dust mass. The dust mass would also change if the grains are porous or not spherical. While we cannot rule out porous grains in our model, studies of meteoritic grains that likely originate from SNe show that they are compact (Molster et al. 2010, pp. 143–201). Since compact grains were also used to estimate the dust mass in SN 1987A, for example, our estimate for G54.1+0.3 at least provides a relative dust mass in relation to those estimated for other SNRs that contain SN-condensed dust.

Another matter of concern is the balance of heating and cooling of the dust in the shell. The IR observations show that only a small fraction of the stellar radiation is reradiated by the dust in the shell. While the available data on the UV absorption properties of $Mg_{0.7}SiO_{2.7}$ grains in particular are incomplete, silicate grains in general are opaque at these wavelengths, so we would expect a much higher fraction of the stellar flux to be absorbed if the total dust mass exceeded a few tenths of the solar mass. However, if the $Mg_{0.7}SiO_{2.7}$ grains are indeed as large as 1 μm (see Section 6.2), their effective absorption per unit mass will be smaller, so the larger dust masses would likely not be in conflict with the inferred low value of the UV optical depth. A more detailed physical heating model will be necessary to resolve these ambiguities and determine whether including these additional effects will significantly alter the estimate of dust mass for G54.1+0.3.

7. Discussion

The fact that the dust in the G54.1+0.3 IR shell shows a fairly uniform spatial mass distribution and no evidence for enhancements at the locations of the stellar sources confirms that the point-like 24 μm excess (Figure 1) does not originate from dust intrinsic to the stars. The map of dust mass surface density is consistent with the scenario in which the stars are heating a shell of dust that condensed from the SN ejecta. The lower mass limit of at least 0.3 $M_{\odot}$ of SN-formed dust derived from the SED fits would be the second largest observationally confirmed dust mass after that of SN 1987A (Matsuura et al. 2015; Dwek & Arendt 2015), assuming that the grains are compact and that the $Mg_{0.7}SiO_{2.7}$ grains are responsible for the observed 21 μm feature and a significant fraction of the mid-IR continuum (additional caveats are discussed in Section 6.4). A large dust mass of $\sim 0.8\,M_{\odot}$ requiring a high condensation efficiency was also inferred for Cas A, accounting for the fact that some of the dust has already been destroyed by the reverse shock (Micelotta et al. 2016). The comparison of the estimated dust mass in G54.1+0.3 with nucleosynthetic yields implies a similarly high condensation efficiency.

The PWN in G54.1+0.3 has not yet been overtaken by the SNR reverse shock, so it is not unexpected that the mass of the

SN-formed dust is still high. Just how much of the observed dust will eventually survive the shock and be injected into the ISM remains uncertain. Micelotta et al. (2016) estimate that only 12%–16% of dust grains will survive the passage of the reverse shock in Cas A. However, this percentage may be higher in the case of Type IIP progenitors that are expected to form larger grains that are not as easily destroyed. For example, in their models that account for the gas-phase chemistry, nucleation, and coagulation of grains, Sarangi & Cherchneff (2015) find that Type IIP SNe tend to form larger grains, especially if the ejecta are clumpy, and that ejecta clumpiness also leads to somewhat higher dust masses and a higher fraction of metallic grains. In addition, if the SN that produced G54.1+0.3 occurred in a low-density bubble produced by the OB association, the reverse shock may be very weak once it encounters the SN-condensed dust that surrounds the PWN, leading to a higher survival rate of grains and a higher eventual input of dust mass into the ISM. This hypothesis will need to be tested with more detailed modeling of the dust destruction by the SN reverse shock.

In order to compare our estimated dust masses with nucleosynthetic yields, we list the yields of C, O, Mg, Al, and Si for different progenitor masses in Table 3, based on the models of Woosley & Heger (2007) and Sukhbold et al. (2016). The table also lists the maximum possible masses of $Mg_{0.7}SiO_{2.7}$, $MgO+SiO_2$, Al_2O_3, and carbon dust that could form in the ejecta, assuming a 100% condensation efficiency. The amount of $Mg_{0.7}SiO_{2.7}$ is limited by the total number of Mg or Si atoms, depending on whether N_{Mg}/N_{Si} is less than or greater than 0.7. The mass of $MgO+SiO_2$ assumes that all Mg and Si in the ejecta are locked up in MgO and SiO_2 and/or one or more forms of Mg_xSiO_{2+x} grains. We compare these values to the lower dust mass limit in the G54.1+0.3 shell, listed in Table 2. The lower mass limit of $\sim 0.25\,M_\odot$ of $Mg_{0.7}SiO_{2.7}$ grains is consistent with nucleosynthetic constraints for a progenitor of at least $\sim 15\,M_\odot$, but this requires an Al_2O_3 mass of $\sim 0.03\,M_\odot$, which corresponds to a progenitor mass of at least $21\,M_\odot$ (see Table 3). However, slightly increasing the mass of $Mg_{0.7}SiO_{2.7}$ would decrease the mass of Al_2O_3 required and therefore lower this limit on the progenitor mass. The next lowest dust mass lower limit of $0.28\,M_\odot$ is for the model of $Mg_{0.7}SiO_{2.7}$ plus carbon dust, and implies a progenitor mass of at least $16\,M_\odot$.

The primary composition of the grains may also offer some clues about the SN progenitor. For example, the $Mg_{0.7}SiO_{2.7}$ grains that make up a large fraction of the dust are characterized by an Mg to Si ratio of 0.7. The sixth column of Table 3 lists the ratio of the numbers of Mg to Si atoms in the ejecta (N_{Mg}/N_{Si}) for different progenitor masses. This ratio is less than unity for progenitor masses of $\sim 27\,M_\odot$ and below. A ratio below unity may explain the formation of the less common magnesium silicate grain species, such as $Mg_{0.7}SiO_{2.7}$, instead of the more common ones like forsterite (Mg_2SiO_4), for which $Mg/Si = 2$. The mass and the composition of the grains in G54.1+0.3 therefore suggest that the mass of the SN progenitor was in the range $16–27\,M_\odot$, consistent with the estimate of Gelfand et al. (2015) and the range of $18–35\,M_\odot$ suggested by the analysis of the stellar cluster by Kim et al. (2013). We note here that a dust condensation efficiency of <100% would lead to a more massive progenitor.

8. Conclusions

We analyzed the 15–500 μm IR emission from a dusty shell of SN-formed dust surrounding the PWN in the SNR G54.1+0.3. We find that the SED, and in particular a spectral feature at 21 μm, is well described by a dust composition of $Mg_{0.7}SiO_{2.7}$ grains, with a secondary component possibly arising from carbon, silicate, or alumina grains. Through a spatially resolved analysis of the IR emission, we derive maps of dust temperature and mass surface density that confirm the scenario in which stellar members of the SN progenitor's cluster are the primary heating sources for the SN dust. The total dust mass resulting from our models is at least $0.3\,M_\odot$, assuming compact grains and a distance of 6 kpc. Self-consistent radiative heating models that invoke a continuous distribution of grain sizes may affect this estimate and allow for a lower dust mass. Nevertheless, the large quantity of dust inferred from our model implies a high dust condensation efficiency, as has been suggested for both SN 1987A and Cas A (Dwek & Arendt 2015; Matsuura et al. 2015; Micelotta et al. 2016). A comparison of the dust mass and composition with nucleosynthetic yields suggests that G54.1+0.3 resulted from a $16–27\,M_\odot$ progenitor. Since the dusty shell has not yet been encountered by the SN reverse shock, the ultimate survival of the dust remains unclear. This study implies that dust can efficiently form in the ejecta of Type IIP SN explosions, and that certain classes of SNe may indeed be significant sources of dust in the universe. Future imaging and spectroscopic observations at high spatial resolution, particularly with the *James Webb Space Telescope*, as well as detailed physical models of dust heating will be necessary to confirm these results.

This work is based in part on observations made with *Herschel*. *Herschel* is an ESA space observatory with science instruments provided by European-led Principal Investigator consortia and with important participation from NASA. This work is based in part on observations made with the *Spitzer Space Telescope*, which is operated by the Jet Propulsion Laboratory, California Institute of Technology, under a contract with NASA. This research includes observations with *AKARI*, a JAXA project with the participation of ESA. Based (in part) on observations made with the NASA/DLR Stratospheric Observatory for Infrared Astronomy (SOFIA). SOFIA is jointly operated by the Universities Space Research Association, Inc. (USRA), under NASA contract NAS2-97001, and the Deutsches SOFIA Institut (DSI) under DLR contract 50 OK 0901 to the University of Stuttgart. E.D. acknowledges the support of NASA 12-ADAP12-0145 for this project. We acknowledge financial support for this work that was provided by NASA through award SOF #04-0167 issued by USRA. We would also like to thank the anonymous referee for providing useful feedback on the manuscript.

References

Aniano, G., Draine, B. T., Gordon, K. D., & Sandstrom, K. 2011, PASP, 123, 1218
Arendt, R. G., Dwek, E., Kober, G., Rho, J., & Hwang, U. 2014, ApJ, 786, 55
Arendt, R. G., Dwek, E., & Moseley, S. H. 1999, ApJ, 521, 234
Barlow, M. J., Krause, O., Swinyard, B. M., et al. 2010, A&A, 518, L138
Begemann, B., Dorschner, J., Henning, T., et al. 1997, ApJ, 476, 199
Bocchino, F., Bandiera, R., & Gelfand, J. 2010, A&A, 520, A71
Cantalupo, C. M., Borrill, J. D., Jaffe, A. H., Kisner, T. S., & Stompor, R. 2010, ApJS, 187, 212

Cherchneff, I., & Dwek, E. 2009, ApJ, 703, 642
Cherchneff, I., & Dwek, E. 2010, ApJ, 713, 1
Chevalier, R. A. 2005, ApJ, 619, 839
Dwek, E., & Arendt, R. G. 2015, ApJ, 810, 75
Dwek, E., & Cherchneff, I. 2011, ApJ, 727, 63
Dwek, E., Galliano, F., & Jones, A. P. 2007, ApJ, 62, 927
Dwek, E., Staguhn, J., Arendt, R. G., et al. 2015, ApJ, 813, 119
Ennis, J. A., Rudnick, L., Reach, W. T., et al. 2006, ApJ, 652, 376
Gall, C., Andersen, A. C., & Hjorth, J. 2011, A&A, 528, A14
Gelfand, J. D., Slane, P. O., & Temim, T. 2015, ApJ, 807, 30
Gomez, H. L., Krause, O., Barlow, M. J., et al. 2012, ApJ, 760, 96
Griffin, M. J., Abergel, A., Abreu, A., et al. 2010, A&A, 518, L3
Henning, T., & Mutschke, H. 1997, A&A, 327, 743
Herter, T. L., Vacca, W. D., Adams, J. D., et al. 2013, PASP, 125, 1393
Hester, J. J. 2008, ARA&A, 46, 127
Houck, J. R., Roellig, T. L., van Cleve, J., et al. 2004, ApJS, 154, 18
Indebetouw, R., Matsuura, M., Dwek, E., et al. 2014, ApJL, 782, L2
Jäger, C., Dorschner, J., Mutschke, H., Posch, T., & Henning, T. 2003, A&A, 408, 193
Kim, H.-J., Koo, B.-C., & Moon, D.-S. 2013, ApJ, 774, 5
Koo, B.-C., McKee, C. F., Lee, J.-J., et al. 2008, ApJL, 673, L147
Kozasa, T., Nozawa, T., Tominaga, N., et al. 2009, in ASP Conf. Ser. 414, Cosmic Dust—Near and Far, ed. T. Henning, E. Grün, & J. Steinacker (San Francisco, CA: ASP), 43
Lu, F. J., Aschenbach, B., & Song, L. M. 2001, A&A, 370, 570
Lu, F. J., Wang, Q. D., Aschenbach, B., Durouchoux, P., & Song, L. M. 2002, ApJL, 568, L49
Matsuura, M., Dwek, E., Barlow, M. J., et al. 2015, ApJ, 800, 50
Matsuura, M., Dwek, E., Meixner, M., et al. 2011, Sci, 333, 1258
Micelotta, E. R., Dwek, E., & Slavin, J. D. 2016, A&A, 590, 65
Michałowski, M. J. 2015, A&A, 577, A80
Molster, F. J., Waters, L. B. F. M., & Kemper, F. 2010, in Lecture Notes in Physics, Vol. 815 ed. T. Henning (Berlin: Springer)
Morris, P., van Dyk, S., Mauerhan, J., Hillier, D. J., & Lang, C. 2010, in ASP Conf. Ser. 425, Hot and Cool: Bridging Gaps in Massive Star Evolution, ed. C. Lietherer et al. (San Francisco, CA: ASP), 277
Ott, S. 2010, in ASP Conf. Ser. 434, Astronomical Data Analysis Software and Systems XIX, ed. Y. Mizumoto, K.-I. Morita, & M. Ohishi (San Francisco, CA: ASP), 139
Owen, P. J., & Barlow, M. J. 2015, ApJ, 801, 141
Poglitsch, A., Waelkens, C., Geis, N., et al. 2010, A&A, 518, L2
Rouleau, F., & Martin, P. G. 1991, ApJ, 377, 526
Sarangi, A., & Cherchneff, I. 2013, ApJ, 776, 107
Sarangi, A., & Cherchneff, I. 2015, A&A, 575, A95
Sibthorpe, B., Ade, P. A. R., Bock, J. J., et al. 2010, ApJ, 719, 1553
Sukhbold, T., Ertl, T., Woosley, S. E., Brown, J. M., & Janka, H.-T. 2016, ApJ, 821, 38
Temim, T., & Dwek, E. 2013, ApJ, 774, 8
Temim, T., Slane, P., Reynolds, S. P., Raymond, J. C., & Borkowski, K. J. 2010, ApJ, 710, 309
Todini, P., & Ferrara, A. 2001, MNRAS, 325, 726
Valiante, R., Schneider, R., Salvadori, S., & Bianchi, S. 2011, MNRAS, 416, 1916
Velusamy, T., & Becker, R. H. 1988, AJ, 95, 1162
Wang, S., Li, A., & Jiang, B. W. 2015, ApJ, 811, 38
Weingartner, J. C., & Draine, B. T. 2001, ApJ, 548, 296
Wesson, R., Barlow, M. J., Matsuura, M., & Ercolano, B. 2015, MNRAS, 446, 2089
Woosley, S. E., & Heger, A. 2007, PhR, 442, 269
Xue, M., Jiang, B. W., Gao, J., et al. 2016, ApJS, 224, 23